JOURNAL OF GEOPHYSICAL RESEARCH, VOL. 104, NO. D24, PAGES 31,781–31,792, DECEMBER 27, 1999

Application of lidar depolarization measurement in the atmospheric boundary layer: Effects of dust and sea-salt particles

Toshiyuki Murayama,[1] Hajime Okamoto,[2] Naoki Kaneyasu,[3] Hiroki Kamataki,[4] and Kazuhiko Miura[5]

Abstract. We intensively observed the atmospheric boundary layer with a polarization lidar, a Sun photometer, and a high-volume sampler at a coastal area of Tokyo Bay. The purpose of the observation is to investigate a phenomenon discovered in the past summer: relatively high depolarization ratio events (≈10% at peak) in the lower atmosphere associated with sea breeze. From the chemical analyses of the simultaneously sampled aerosols, we found that the depolarization ratio might be related to crystallized sea salt and dust particles. A boundary structure was clearly revealed by the depolarization ratio in the lower atmosphere, which might correspond to the mixed layer (the internal boundary layer) or the sea breeze in which crystallized sea salt and/or dust particles were diffused. We also presented the first numerical calculation on the depolarization ratio of the cubic particles to apply crystallized sea-salt (NaCl) particles by the dipole discrete approximation (DDA) method: the calculation yields 8–22% of depolarization ratio for the effective size larger than 0.8 μm at the investigated wavelength (532 nm).

1. Introduction

We have routinely observed the troposphere, mainly to study the atmospheric boundary layer (ABL) (also referred as the planetary boundary layer (PBL)), with a lidar at Tokyo University of Mercantile Marine (TUMM) (35°40′N, 139°47′E) since 1993. Our observation site is located in the center of Tokyo and close to Tokyo Bay, as shown in Figure 1. A large amount of aerosols is locally emitted from anthropogenic origins and greatly affects the local air quality and visibility. This site is suited for the study of the urban atmospheric boundary layer, the boundary layer aerosols, the air pollution meteorology, and the sea-land breeze circulation. Aerosols in ABL, except in spring when Asian dust exists, normally dominate the optical thickness of the atmosphere in this area. Therefore the optical property of the aerosols in the urban ABL is one of the most important targets to estimate the direct and indirect effects of the tropospheric aerosols on the radiation budget.

The lidar depolarization technique has been extensively applied to cloud research, e.g., to discriminate the phase of clouds (i.e., water or ice clouds) [*Sassen*, 1991, 1999]. However, the application of this technique to the tropospheric aerosol is relatively rare [*Sassen*, 1999]. We explored the importance of the lidar depolarization technique in the boundary layer meteorology and characterization of boundary layer aerosols. One of the advantages of the boundary layer study is that we can relate lidar data to meteorological data and in situ measurements of aerosols at the ground level, although the boundary layer aerosols are mixed with various kinds of aerosols and therefore complex. For the upper atmosphere case we need radiosonde observations and airborne sampling of aerosols for a direct comparison with lidar data, which would be highly expensive.

In this paper we define the directly observed total depolarization ratio as δ_t, which includes both depolarizations from molecules δ_m and from particles δ_p. We use here the definition of δ_t defined as $\delta_t \equiv P_\perp/P_{//}$, where $P_\perp$ and $P_{//}$ are the components of backscattered light powers polarized perpendicular and parallel, respectively, to the direction of the linearly polarized transmitted laser. Extraction method of δ_p from δ_t is mentioned in section 3.5.1. Normally, the value of δ_t in the mixed layer (ML) ranges from 2 to 10% in this area. We found that δ_t tends to decrease as the relative humidity (RH) increases [*Murayama et al*., 1996]. Much higher δ_t value of 10–30% was often observed for Asian dust events in spring, which contain large and irregular yellow-sand particles [*Iwasaka et al*., 1988; *Murayama et al*., 1998a]. We also observed high δ_t events (≈10%) due to local dust in the ABL on windy days. Clear enhancement of the δ_t (≈5%) in the ML has been often observed in wintertime, which might be caused from the soil dust and/or urban aerosols under low RH [*Murayama et al*., 1998b].

As we have reported [*Murayama et al*., 1996, 1997], the δ_t in the lower atmosphere (LA) suddenly increases in the afternoon when the sea breeze becomes dominant and decreases rapidly in the evening. We proposed a hypothesis that it is related to sea-salt crystallization under low RH because the sea-salt particles are the main composition delivered by the sea breeze, and the observed behavior of δ_t seemed to correspond to the deliquescence of sea-salt particles. To validate this hy-

[1]Tokyo University of Mercantile Marine, Koto, Tokyo, Japan.
[2]Kashima Space Research Center, Communications Research Laboratory, Kashima, Ibaraki, Japan.
[3]National Institute of Resources and Environment, Tsukuba, Ibaraki, Japan.
[4]Tokyo Metropolitan Research Institute for Environmental Protection, Koto, Tokyo, Japan.
[5]Department of Physics, Science University of Tokyo, Shinjuku, Tokyo, Japan.

Paper number 1999JD900503.
0148-0227/99/1999JD900503$09.00

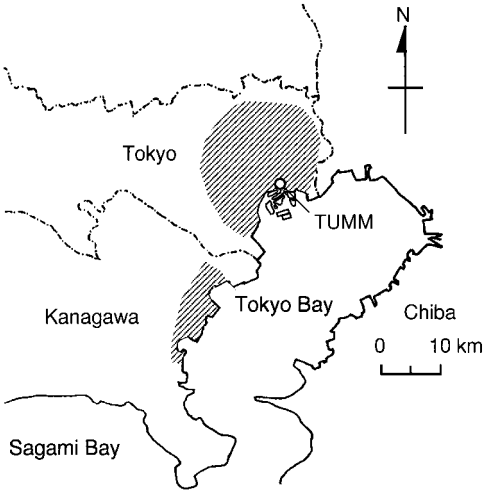

Figure 1. Location of the observation sites, Tokyo University of Mercantile Marine (TUMM) (35°40′N, 139°47′E). The shaded areas denote roughly the most urbanized areas.

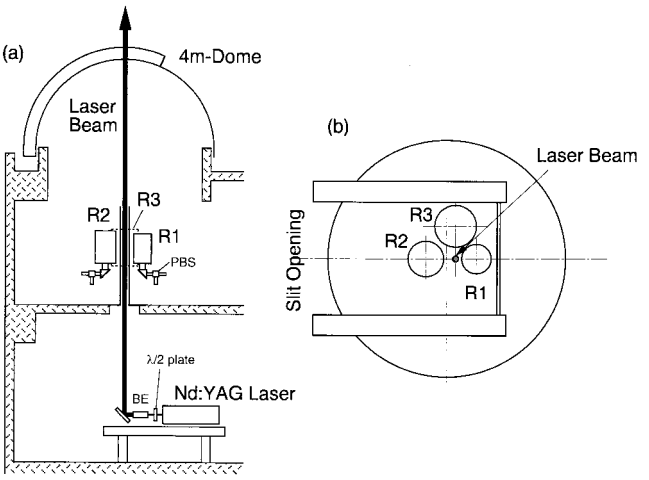

Figure 2. Optical layout of the TUMM lidar system: (a) cross-sectional view and (b) top view over the dome. BE and PBS denote a beam expander and polarizing beam splitters.

pothesis, we made a more systematic observation on this phenomenon, which included a high time-resolved sampling of surface aerosol in the summer of 1996. Part of the results and preliminary discussions were given in conferences [*Murayama et al*., 1998b, c].

2. Experimental and Analytical Procedures

We intensively observed the ABL with a lidar, a Sun photometer, and a high-volume sampler from July 16 to 19, 1996. During this period the Tokyo area was covered by anticyclone, and the weather was fine. In this section we describe the details of instrumentation and the procedure of analyses to derive the optical and chemical properties of aerosols.

2.1. Lidar System and Data Analysis

We used the TUMM lidar system operated at the wavelength of 532 nm, which has two polarization receivers to expand the dynamic range of detection. At an urban site such as Tokyo we need an extremely wide dynamic range of detection due to the constantly hazy condition in the LA (a general description of lidar is given by *Measures* [1984]). The specifications of the present lidar system are given in Table 1. The lidar system is located about 35 m above the mean sea level (msl). The schematic layout of the present system is shown in Figure 2. The laser is vertically emitted through an astronomical dome. Under the opening slits of the dome, receiving telescopes are arranged as shown in Figure 2b. Receivers, R1 (near-field receiver) and R2 (far-field receiver), are supported by the fork mounts on the tripods, and R3 is mounted on an optical bench. R3 is used for multiple purposes, i.e., as Raman channels for nitrogen and water vapor molecules or as a 1064 nm Mie scattering channel, etc. The data obtained by R1 and R2 are discussed in this paper. The arrangement of the receiving optics in R1 and R2 was similar to the one described in a previous paper [*Murayama et al*., 1996]. We set the field of view (FOV) for R1 and R2 as 3 and 1 mrad, respectively, during the observation. So-called the overlapping factor $Y(z)$ [*Measures*, 1984] between the laser beam and the FOVs of each, receivers became unity when z, the range from the lidar, was 200 m for R1 and 700 m for R2, respectively. The $Y(z)$ of R1 was empirically evaluated down to $z = 116.25$ m from the comparison of backscattering intensities obtained by changing the FOV of R1 between 3 and 5 mrad in a short period. The signals were recorded up to 7 km with 7.5 m resolution. The lidar

Table 1. Specifications of the TUMM Lidar System (December 1998)

	Transmitter		
Laser	Q-SW Nd:YAG (532 nm, 1064 nm)		
Pulse energy	10–20 mJ in typical tropospheric observation, 250 mJ at max for 532 nm		
Pulse width	10 ns		
Repetition rate	10 Hz		
Beam divergence	<0.2 mrad		
	Receivers		
	R1	R2	R3
Effective diameter	20.3 cm	25.4 cm	30.4 cm
Field of view	1–6 mrad	0.5–4 mrad	1–3.5 mrad
Main use	near-field polarization (532 nm)	far-field polarization (532 nm)	Raman (N_2, H_2O), 1064 nm
Detectors	PMT (Analog)	PMT (Analog)	PMT (analog and photon counting)

Type used for receivers is Schmidt-Cassegrainian (F-Number: 10).

signals were averaged every 10 min (6000 shots) by a digitizing storage oscilloscope with 8-bits resolution and transferred into a personal computer automatically. We connected both the backscattering intensity and the depolarization ratio profiles obtained by two receivers at $z = 750$ m.

The total depolarization ratio δ_t was determined from the ratio of the detector signals of copolarization and cross-polarization channels by multiplying it by the gain ratio of the corresponding detectors. The gain ratio was determined by rotating a half-wavelength plate located at the laser output or by using unpolarized light. The error was ±5%, which corresponds to ±5% relative error in determination of δ_t. Another factor of the error in δ_t could come from the incomplete separation of the linear polarization due to the receiving optics, which was estimated to be less than 1%. This error should appear as a constant offset in the observed δ_t. However, we did not subtract this unknown error throughout the presented data and analysis.

We derived the extinction coefficient of aerosols by using the algorithm of *Fernald* [1984] with the U.S. Standard Atmosphere (U.S. GPO, Washington, D.C., 1976). The molecular backscattering and extinction coefficients at 532 nm are given as 1.59×10^{-3} km^{-1} sr^{-1} and 1.33×10^{-2} km^{-1}, respectively, at sea level in U.S. Standard Atmosphere (15°C, 1 atm) [*Measures*, 1984]. The result of the analysis significantly depends on the ratio of the extinction coefficient (σ) to backscattering coefficient (β), so-called the lidar ratio $S_a(=\sigma/\beta)$. Therefore we need an adequate choice of S_a. This is accomplished by simultaneous measurement with lidar and Sun photometer: the comparison between the optical thicknesses derived from the lidar (at 532 nm) and the Sun photometer (at 500 nm) can provide an average S_a in the troposphere [*Takamura et al*., 1994; *Murayama et al*., 1997]. We also need a sufficient signal to noise ratio of the backscattering intensity at the farside boundary range and a good estimation of the boundary value to apply this method. Here we chose a fixed boundary condition at an aerosol-free height and a constant S_a as follows: the scattering ratio (SR) was taken as 1.2 at the boundary range (height) $z = 5$ km, where SR is defined as

$$\mathrm{SR} = \frac{\beta_m + \beta_p}{\beta_m}, \tag{1}$$

where β_m and β_p are the backscattering coefficients of air molecules and particles, respectively. S_a was taken as 50 sr, which was chosen to reproduce the optical thickness derived from the Sun photometer. This is a typical value of S_a in the troposphere [*Takamura et al*., 1994]. We fixed the boundary condition and S_a throughout the present lidar analysis. The error estimation due to the boundary condition and constant S_a in lidar analysis, i.e., the dependence of S_a on the lidar-derived optical thickness and extinction coefficient, is discussed in section 3.2.

2.2. Sun Photometer

We used a portable (manual) Sun photometer (model MS-120; EKO, Tokyo, Japan), which can retrieve the aerosol optical thicknesses τ at the wavelengths of 368, 500, 675, and 778 nm from the measurements of direct solar radiation. The apparatus constants E_λ given by the manufacturer were used for the present analysis, and those relative errors $\Delta E_\lambda/E_\lambda$ were considered to be within ±5% [*Miura et al*., 1997]. The errors led to the error of the optical thickness $\Delta\tau$ given by $\Delta E_\lambda/(E_\lambda m)$ without depending on τ, where m is the air mass at the measurement. The wavelength dependence of τ is empirically described by the following equation [*Angström*, 1961]:

$$\tau(\lambda) = \beta_0/\lambda^\alpha, \tag{2}$$

where $\tau(\lambda)$ is the aerosol optical thickness at the wavelength of λ in micrometers, and β_0 and α are so-called turbidity coefficient and wavelength exponent, respectively. The measurements of Sun photometer and filter sampling mentioned below were done on the rooftop of the building where the lidar system has been located.

2.3. Filter-Sampling and Chemical Analyses of Aerosols

During the observation, suspended aerosols were simultaneously collected by a dichotomous high-volume sampler (model 130, Kimoto, Osaka, Japan). The sampler consists of an impactor and a backup filter holder. Coarse particles (diameter $d > 2$ μm) are collected by the slit-orifice impactor (50% cutoff diameter: 2 μm) with a quartz fiber filter placed on the plate, whereas fine particles ($d \leq 2$ μm) are collected by a backup quartz fiber filter. Adoption of this separation diameter is based on the typical in the size distribution of tropospheric aerosols, which is bimodal with a minimum around 2 μm in diameter [*Hidy*, 1984]. The large and fine particles (modes) are generally originated from the natural and anthropogenic sources, respectively. The sampling rate of the device is 400 L/m, which enables relatively high time-resolved sampling. We replaced the filters manually to follow the change of the atmospheric conditions. The replacement time intervals varied from 2 to 7 hours. The quartz-fiber filters (Pallflex 2500QAT-UP) used in the sampling were treated with heat (850°C) in air for 90 min before use to reduce carbonaceous blanks.

From the filter samples, concentrations of water-soluble components, such as SO_4^{2-}, NO_3^-, Cl^-, NH_4^+, Na^+, Ca^{2+}, K^+, and Mg^{2+}, were determined by ion chromatography at the Tokyo Metropolitan Research Institute for Environmental Protection, and an analysis of carbonaceous components was made at the National Institute of Resources and Environment. Elemental carbon (EC) and total carbon (TC) were determined by a combustion technique [*Ohta and Okita*, 1984]. Organic carbon (OC) was evaluated by subtracting EC from TC.

The meteorological data, i.e., the temperature, relative humidity, wind speed and direction, and solar radiation, were recorded on the rooftop of another building (35m above msl) at TUMM. Meteorological and air pollution data (PM_{10}, NO_x, O_3, etc.) at the local-government air pollution monitoring stations (Ariake and Ohjima stations located 3.7 km south and 4.0 km northeast of TUMM, respectively) are also used as supplement in the present discussion.

3. Results and Discussions

In this section we describe the general features of the observations and discuss the results of lidar, Sun photometer, and the components of sampled aerosols with reference to the surface meteorological and air pollution data. From the data recorded at the air pollution monitoring stations and from the results of our measurements, surface air was more polluted on July 18 and 19 than on July 16 and 17.

3.1. Dynamics of ABL Revealed by Lidar Measurement

The surface meteorological data are shown in Figures 3a and 3b, where air temperature and relative humidity were provided

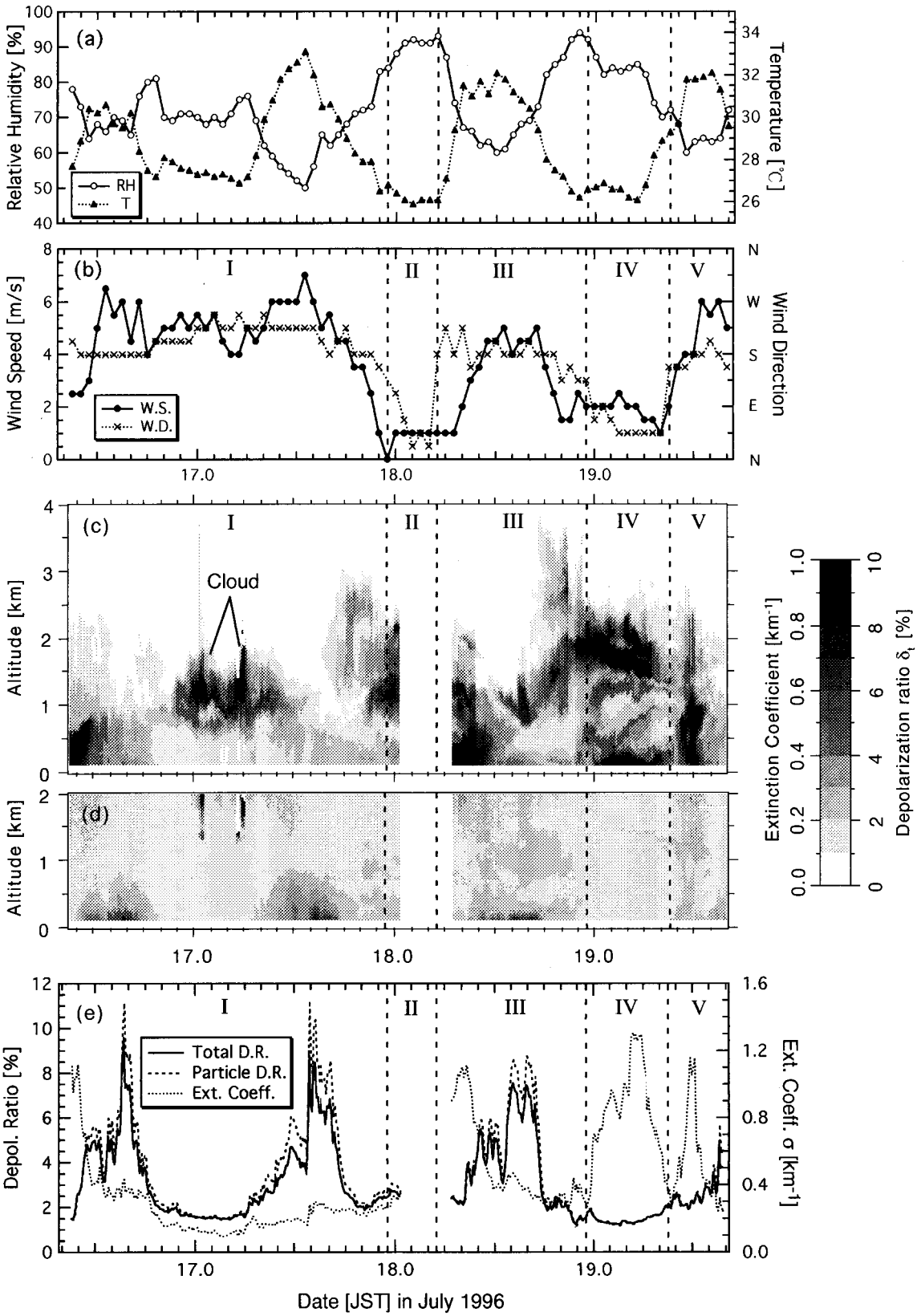

Figure 3. Temporal changes of surface meteorological data and lidar data on July 16–19, 1996: (a) temperature and relative humidity at Ariake, (b) wind speed and direction at TUMM, vertical profiles of the extinction coefficient (c) and total depolarization ratio (d), and (e) total and particle depolarization ratios and extinction coefficient at lower atmosphere (~150 m above msl). Periods I–V are marked according to sea and land breezes (see text).

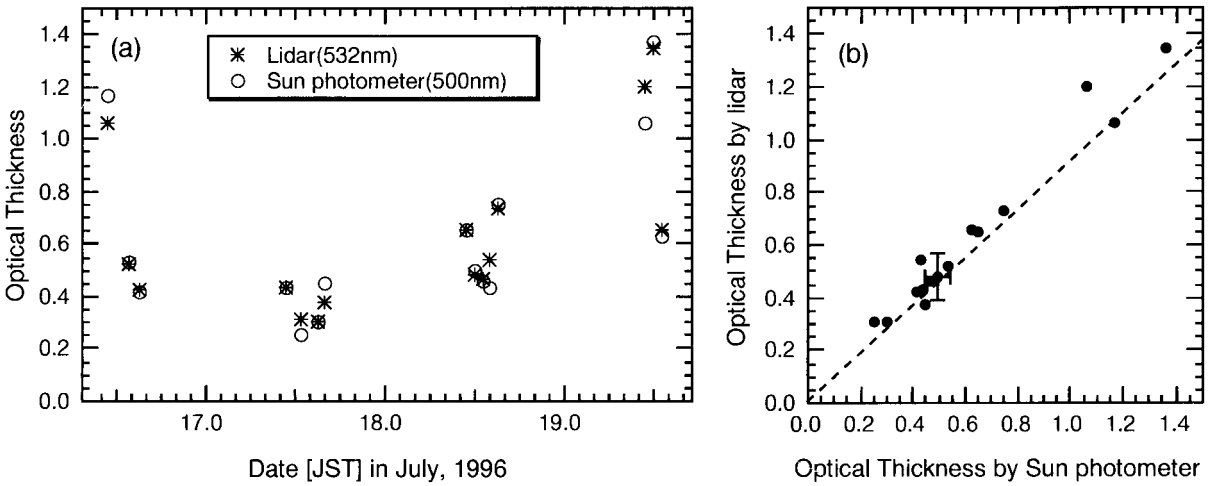

Figure 4. Optical thicknesses derived from the Sun photometer and the lidar measurements: (a) temporal change and (b) relationship between both values. The dashed line in Figure 4b shows the relationship of the averaged wavelength exponent $\alpha = 1.50$ obtained from the Sun photometer measurement (see text).

from the Ariake station because the hygrometer at TUMM was not functioning properly during the period. The surface wind system in the area in the summertime is generally governed by sea breeze in the daytime and week land breeze in the nighttime. We divided roughly the periods in Figure 3 by I to V according to sea (southward) and land (northward) breezes. Sea-breeze episodes are denoted by periods I, III, and V. Sea breeze blew exceptionally during the night of July 16 through the morning of July 17 (period I). Periods II and IV correspond to land breeze episodes.

The temporal variations of extinction coefficient and depolarization ratio δ_t from July 16 to 19, 1996, are shown in Figures 3c and 3d. Note that the lidar measurement was temporally interrupted from 0038 to 0642 LT, July 18, because of the appearance of low-level clouds. The δ_t profiles over 2 km are omitted in Figure 3d due to the low signal to noise ratio and the smallness of δ_t about 2% even under high aerosol-loading conditions in summer. The reason for small δ_t in the aerosol layer in higher altitude is considered to be as follows: Most of these aerosols are probably anthoropogenic and hygroscopic. Therefore aerosols afloat in the atmosphere are small and/or hygroscopically grown and they tend to show sphericity. This tendency does not hold to Asian dust frequently observed in spring because the dust is nonspherical and less hygroscopic.

The figures show that the present observation reconfirmed the phenomenon we reported [*Murayama et al*., 1997]; that is, (1) the depolarization ratio in the LA often increased up to about 10% when the sea breeze developed early in the afternoon, and (2) the depolarization ratio decreased rapidly in the evening. In addition, the lidar observation revealed diurnal dynamics of ABL in the area as mentioned below.

In Figure 3c we found that the LA was hazy and highly polluted during the early stages of sea breeze episodes (periods I and III) and land breeze episode (IV). Land breeze should deliver more polluted air from the urban area off the coast. Because of exceptional continuous sea breeze in period I the LA on the morning of July 17 was clear. In those high-polluted periods the depolarization ratio was low. This is expected from dominant urban aerosols that have a finer size and hygroscopic nature. As the ML and sea breeze developed and the RH near the surface decreased around noon, the hazy condition was rapidly dissipated. At the same time, the top of the relatively high δ_t layer rose up to several hundred meters, presumably coinciding with the development of ML. Since our measurement was conducted close to the coast of Tokyo Bay and was affected strongly by the sea breeze in summer, it should be referred to as the effect of the internal boundary layer (IBL) [*Garrat*, 1992] as well as ML. The height also seems to correspond to the height of the sea breeze layer [*Banta et al*., 1993]. This boundary structure that appeared in δ_t should be investigated by a simultaneous radiosonde observation. In the afternoon of July 17 and 18, dense aerosol layers appeared over 1 km. These might be a return flow of the sea breeze, which was transported from more developed ML in the interior. The mechanism was investigated by the lidar network observation of the ML over Tokyo [*Kai et al*., 1998]. Another possible source is the long-range-transported aerosols. Complicated behavior of the multiple layers in the higher ABL, i.e., oscillation and convergence, was also observed during the night from July 18 to 19.

Temporal variations of the extinction coefficient and depolarization ratios δ_t and δ_p, at the height of 116.25 m ($\approx$150 m above msl), are shown in Figure 3e. High δ_t events appeared when the RH was low and the sea breeze was dominant. This behavior was observed prominently, except on July 19. One marked feature is two-stage increases of δ_t, one in the morning and the other large (or sudden) one in the afternoon. A slight increase of extinction coefficient was also recognized at the second peak of δ_t; it is most prominently seen in the afternoon of July 17 under relatively clear air conditions. This rapid change seems to suggest the passage of the sea breeze front [*Nakane and Sasano*, 1986]. Details are discussed in section 3.5.

3.2. Optical Thickness Derived From Lidar and Sun Photometer

Figure 4 shows the comparison of the optical thicknesses (also referred to as optical depth (OD)) obtained by the lidar and the Sun photometer. To evaluate the lidar optical thickness, we integrated the derived extinction coefficients $\sigma(z)$ below 5 km with respect to range z, assuming the uniform distribution of σ below $z = 116.25$ m. The fixed value of the

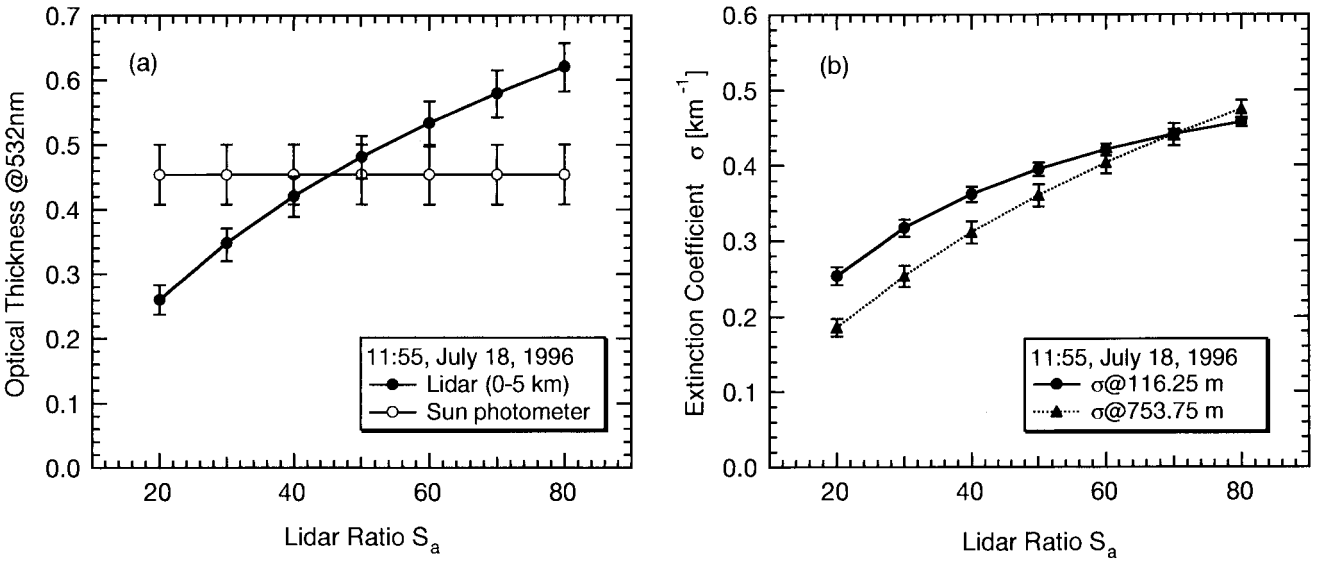

Figure 5. Examples of S_a dependence of (a) optical thickness and (b) the extinction coefficients at different heights derived from lidar analysis.

lidar ratio, $S_a = 50$, is chosen to reproduce the optical thickness derived from the Sun photometer. The averaged wavelength exponent α derived from the Sun photometer measurement was 1.50. The dashed line in Figure 4b indicates the corresponding relation when we take into account the difference between the observation wavelengths of lidar (532 nm) and the Sun photometer (500 nm). A reasonable coincidence of both optical thicknesses in Figure 4b suggests the following: (1) the optical thickness was mostly caused from the aerosols in the lower troposphere, and (2) the lidar analysis is less sensitive to the choice of the boundary condition and the lidar ratio in the turbid atmosphere as the present case (OD = 0.3–1.4).

We examined the dependencies of the optical thickness and the extinction coefficients on S_a as shown Figure 5. The error bars represent expected uncertainties due to the plausible range of the boundary condition: the error of assumed SR as 1.2 at 5 km in altitude is estimated to be ± 0.1, which corresponds to $\pm 50\%$ error in σ. In this example the uncertainties in the OD and the lower extinction coefficient caused by the plausible uncertainties of the boundary condition (1.2 ± 0.1) and lidar ratio (50 ± 10) remain less than $\pm 20\%$ and $\pm 10\%$, respectively. (This uncertainty of OD is shown in Figure 4b.) Figure 5b shows that the retrieved extinction coefficient at the lower height (near-field solution, in this case at $z = 116.25$ m) is less dependent on the S_a value than that at the higher one ($z = 753.75$ m). This is expected from the nature of the backward solution in the inversion method [*Klett*, 1981; *Sasano and Nakane*, 1984]. This stability of the near-field extinction coefficient will benefit the discussion between the mass concentration of aerosol and the extinction coefficient as given in section 3.4.

3.3. Chemical Feature of Surface Aerosols

Mass concentrations of water-soluble and carbonaceous components in fine and coarse particles are shown in Figure 6. The carbon components, especially EC, were one of the large components in the fine particles. We found that SO_4^{2-}, EC, and NH_4^+ populated in the fine mode rather than in the coarse mode. On the contrary, Ca^{2+}, Na^+, Mg^{2+}, and Cl^- mostly populated in the coarse mode. A large concentration of Ca^{2+} (C; hereinafter we refer to fine and coarse particles as F and C), about several micrograms, was observed.

Ion equivalent ratios (IER) of the water-soluble components in fine and coarse particles are shown in Figure 7. IER should be more effective than mass concentration to determine the chemical forms of the aerosols and the relationship with δ_p in the LA, because the observed value of δ_p reflects contributions from all kinds of aerosols. So the higher value of δ_p implies that the percentage of nonspherical particles is higher. The ion balance was not well held especially in the coarse particles: the sum of molecular equivalence of cations is greater than that of anions except on July 19. This fact may be related to the large concentration of Ca^{2+}(C). We have found relatively apparent diurnal changes in the following components: Ca^{2+}, SO_4^{2-}, EC in the fine particles, and Na^+, Cl^-, Ca^{2+}, NO_3^-, SO_4^{2-}, Mg^{2+} in the coarse particles. Among them, the Ca^{2+} and Na^+ in the coarse particles are considered as indices of soil and sea-salt particles, respectively, which can cause high depolarization. Each pattern of the temporal changes for the Ca^{2+}(C), Ca^{2+}(F), and Na^+(C) is different from others, and we discuss them in the light of the behavior of δ_p in the LA in section 3.5.2.

3.4. Extinction Coefficient and Mass Concentration

We compared the lidar-retrieved extinction coefficient with the mass concentration of PM_{10} at air pollution monitoring stations, as shown in Figure 8. PM_{10} is defined in the ambient air quality standard in Japan as the mass of aerosols sampled through 10-μm-cut-size separator. In the stations, PM_{10} is measured with beta-ray absorption-type automated monitors every hour; the resolution of the measurement is about ± 10 $\mu g/m^3$. Although the measurement of PM_{10} was conducted about 4 km apart from TUMM, the trend of temporal changes in the concentration generally agree with that of the extinction coefficient at 150 m above msl. The ratio of the extinction coefficient (σ) to the mass concentration of PM_{10} (ρ) varies 3–12 m^2/g, and the average value is 6.5 ± 2.0 m^2/g (we used the Ohjima value as ρ because it has less scatter than the Ariake value). This value is consistent with the reported values of the

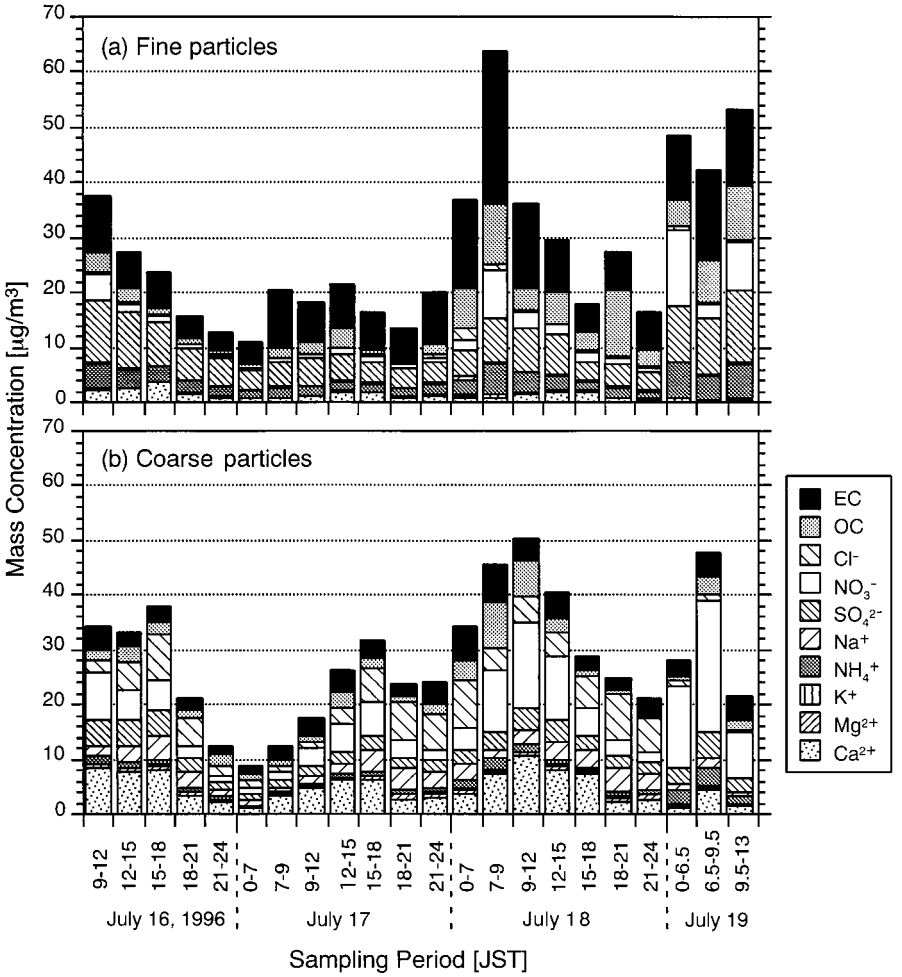

Figure 6. Mass concentrations of soluble components and organic (OC) and elemental (EC) carbons in (a) fine (≤ 2 μm) and (b) coarse (>2 μm) particles during the observation.

ratio of the mass concentration to the light-scattering coefficient (specific scattering coefficient) for urban hygroscopically grown aerosols [*Charlson et al*., 1969, 1992; *Friedlander*, 1977; *Hoff et al*., 1996]. The specific scattering ratio should vary depending on RH and chemical compositions of aerosols. The scattering coefficient of aerosols is usually measured by the nephelometer. The lidar-derived extinction coefficient is the sum of the scattering and absorption coefficients. Thus σ/ρ is expected to be higher than the specific scattering coefficient for the EC-rich aerosols as in the present case. Considering the uncertainties in the lidar-derived extinction coefficient and the mass concentration of aerosols in the present methods, we restrict this discussion to show the potential ability of lidar for environmental monitoring. A reasonable correspondence of lidar-retrieved extinction coefficient and surface-level aerosols mass concentrations might be achieved by the following reasons: (1) the extinction coefficient derived by the Fernald method is relatively reliable at a lower altitude, as discussed in section 3.2, and (2) there is not much difference in PM_{10} on the surface and at 150 m above msl because the surface inversion should be weaker in summer.

The total mass concentration of surface aerosols rebuilt by summing up all the components analyzed is also indicated in Figure 8 as SP. The PM_{10} is well reconstructed by SP except on July 19. This ensures that we can discuss the chemical compositions of surface aerosols in terms of the results of the present chemical analyses.

3.5. Diurnal Change of Depolarization Ratio in the Lower Atmosphere

In this section we discuss the marked change of the depolarization ratio in the LA. At first we mention the derivation of the particle depolarization ratio δ_p from the total depolarization δ_t, then we consider the relationship between δ_p and the chemical components of aerosols.

3.5.1. Particle depolarization ratio. The total depolarization ratio δ_t reflects the molecular depolarization ratio δ_m and particle depolarization ratio δ_p. The particle depolarization δ_p is expressed by the following equation:

$$\delta_p' = (\mathrm{SR}\ \delta_t' - \delta_m')/(\mathrm{SR} - 1) \tag{3}$$

where $\delta' = \delta/(1 + \delta)$. We evaluated the particle depolarization δ_p at $z = 116.25$ m by using (3) and the molecular depolarization ratio δ_m given as 1.4% [*Young*, 1980; H. Adachi, private communication, 1996]. The result was already presented in Figure 3e. As expected from (3), δ_t comes close to δ_p as SR increases [*Murayama et al*., 1996]. In fact, the difference between δ_t and δ_p is small in Figure 3e. The absolute error due to the uncertainty of S_a is estimated to be about $\pm 1\%$ at the maximum of δ_p.

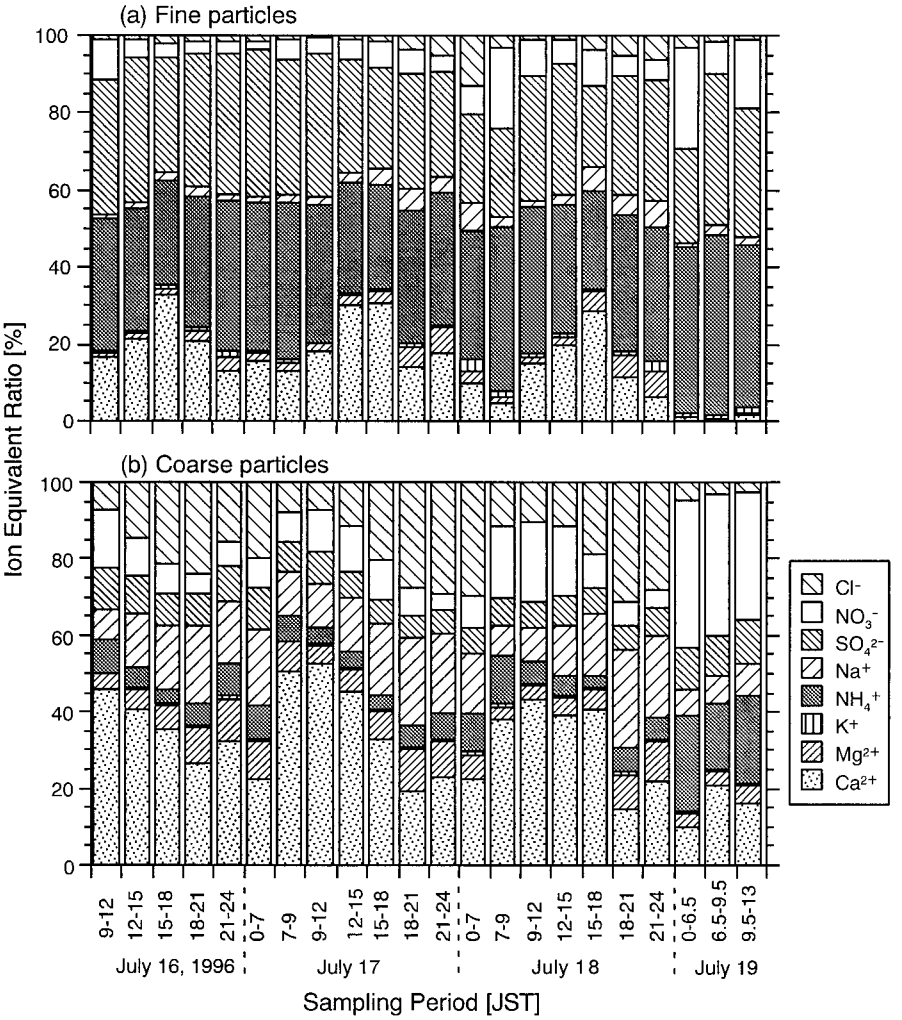

Figure 7. Ion equivalent ratio in the fine and coarse particles during the observation.

3.5.2. Relationship with chemical components of surface aerosols. To interpret the marked diurnal variation of δ_p in LA, the behavior of some chemical components in surface aerosols was investigated. Soil particles and sea-salt particles, i.e., candidates of nonspherical particles, are indicated by Ca^{2+} and Na^+, respectively. In Figure 9, temporal variations of IER for Na^+(C) (Cl^-(C) is similar as Na^+(C)), Ca^{2+}(F), and Ca^{2+}(C) in surface aerosols are plotted with that of δ_p in the lower troposphere. We can see a remarkable diurnal pattern of δ_p; showing small peaks in the morning and a sudden increase around 1300–1400 Japan standard time (JST) followed by a rapid decrease in the evening. On the other hand, the three

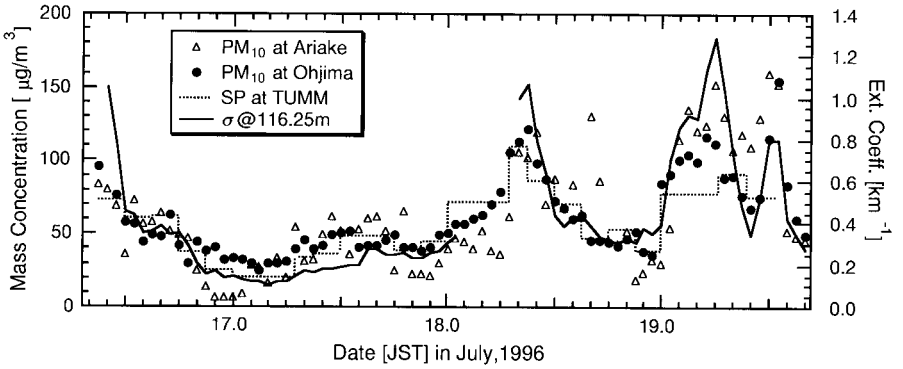

Figure 8. Temporal changes of the extinction coefficient at about 150 m above msl and the PM_{10} concentrations at ground level. PM_{10} data were given by the local air pollution stations, Ariake and Ohjima. The indicated extinction coefficients are averaged over an hour. The dotted curve shows the total mass concentration (SP) derived from the all chemical analyses (soluble plus carbons) of the filter-sampled aerosols.

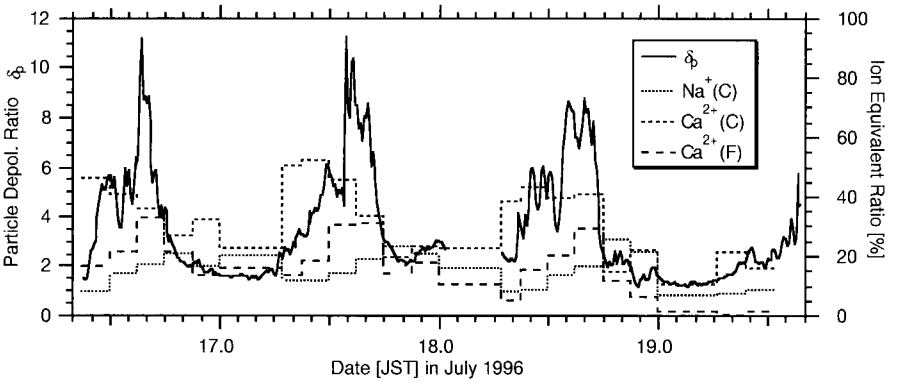

Figure 9. Temporal changes of the particle depolarization ratio and ion equivalent ratios of Na^+ and Ca^{2+} in fine and coarse particles. F and C stand for fine and coarse particles.

components mentioned have diurnal variations in IER with different phases. The peak of Ca^{2+}(C) in IER appeared from early morning to noon, while that of Ca^{2+}(F) appeared at some point in the morning. IER of Na^+(C) became maximum later than that of Ca^{2+}(F) and Ca^{2+}(C). The peaks of Ca^{2+}(C) and Ca^{2+}(F) appear to correspond to the structure of δ_p in the daytime of July 16–18: the smaller peak in the morning and the larger one in the afternoon. The rising of Na^+(C) also coincide with the second peaks of δ_p.

Considering the above behavior of IER of Ca^{2+}(F, C) and Na^{2+}(C) and the meteorological data as shown in Figures 3a and 3b, we can reach the following scenario of observed change of δ_p: the first peak in δ_p was caused by the dust particles from local sources, while the second, larger peak was caused by dust particles and crystallized sea-salt particles, which were delivered by the strong sea breeze. Soil particles are not hygroscopic and nonspherical and should cause high depolarization without depending on RH. Contrary to the soil particles, sea-salt particles (mainly NaCl particles) have a hygroscopic nature and a hysteresis with RH: once the sea-salt particles are generated in solid phase, the phase does not change until 75% RH (deliquescence). On the other hand, the wet sea-salt particles might remain at a supersaturated droplet phase until RH reached 45–48% [*Winker and Junge*, 1971; *Tang et al*., 1977; *Tang*, 1996]. Taking into account the behavior of Na^+(C) and the fact that the high δ_p occurred under low RH, we can expect the contribution of crystallized sea-salt particles to the second peak of δ_p. We regard as an open question whether sea-salt particles were generated in solid phase or partially crystallized during delivery by wind in the present experiment. However, it is clear that crystallized sea-salt particles cause a high depolarization due to the nonsphericity mentioned in the following section. A rapid decrease of δ_p in late afternoon is anticipated from a decrease of the dust particles and an increase of the wet sea-salt particles. The hygroscopic growth of the urban aerosols and generation of the small secondary particles under high RH might decrease δ_p.

As for the sources of soil or dust particles containing Ca^{2+}, the following origins are possible candidates: (1) road dust, soil and cement particles from the construction cites, and/or industrial area located southward of TUMM; (2) soil or dust particles transported for relatively long distance from the urban and reclaimed area extending into Tokyo Bay. The generation mechanism of wind-driven soil and sea-salt particles is strongly related to speed [*Gillette et al*., 1974, 1978; *Blanchard and Woodcock*, 1980]. As sea breeze becomes stronger, more soil and sea-salt particles, which have relatively larger size, might be generated. At the same time, the polluted air must be swept away inland.

To obtain more solid evidence of the effect of sea-salt and soil particles on the observed high δ_t events, we need a more direct analytical method, e.g., collection of the suspended aerosols by a cascade impactor and the morphological and multielement analysis with scanning electron microscope (SEM) and energy dispersive X ray (EDX) analyses [e.g., *Miura et al*., 1991].

4. Depolarization Ratio Due to Crystallized Sea-Salt Particles

As discussed in section 3, we consider dust and/or crystallized sea-salt particles as the main sources of observed depolarization in ABL. Here we concentrate on sea-salt particles since the shape of dry sea-salt particles, i.e., NaCl particles, is known to be cubic, and their refractive index is also experimentally determined, i.e. $m = 1.5443 + 0.0i$. Contrary to sea-salt particles, dust particles are known to be highly irregular and thus prevent realistic modeling of light backscattering theoretical calculations. Therefore it is advisable to study the backscattering signatures of homogeneous cubic particles by theoretical calculations as a general problem in light scattering by nonspherical particles. Real sea-salt particles might not be always perfectly cubic (see SEM images of NaCl particles [e.g., *Perry et al*., 1978]), and we treat crystallized sea-salt (NaCl) particles as perfectly cubic as a first approximation. To our knowledge, this is the first theoretical study on light scattering by cubic particles.

Dry NaCl particles are often treated as typical irregular particles that are easily artificially generated in the laboratory [*Bohren and Huffman*, 1983]. First, we briefly look into the experimental aspects of the light scattering by NaCl particles to see how much depolarization effect is expected before describing our results in numerical calculations.

4.1. Light-Scattering Experiments on NaCl Particles in Laboratory

The depolarization ratio in the closely backward scattering for dry NaCl particles obtained in the previous laboratory measurements range from 0.25 to 0.33 [*Cooper et al*., 1974; *Perry et al*., 1978; *Quinby-Hunt et al*., 1997]. *Quinby-Hunt et al*.

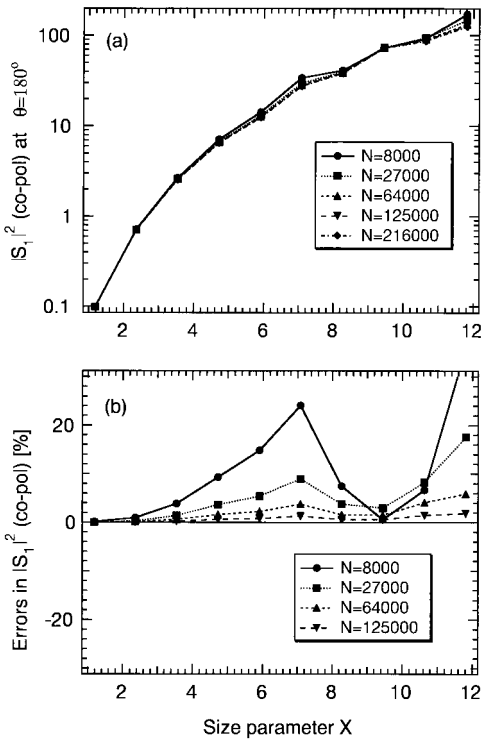

Figure 10. (a) Backscattering radiances for copolarization by the dipole discrete approximation (DDA) for cubic sea-salt particles with given N and X. As a refractive index, $m = 1.54 + 0.01i$ at the wavelength of 0.532 μm is used. (b) Relative errors for N where the solutions for N = 216000 is used as references.

[1997] showed that light scattering by wet NaCl particles was so well described, based on Mie theory, as to derive size distribution and refractive index. *Cooper et al*. [1974] showed that a nonzero depolarization ratio from 0.06 to 0.12 is caused by NaCl droplets. They concluded that depolarization measurements are not unambiguous indicators of sphericity or nonsphericity under some conditions. Thus even if the sea-salt particles are not perfectly crystallized, they might cause nonzero depolarization.

4.2. DDA Calculation of Depolarization Ratio for Cubic Particles

Recently, considerable progress has been made to solve light-scattering problems for nonspherical shapes. T-matrix is one such method, and it is widely used because of its high accuracy and the fact that it can be applied for a particle whose size parameter X ($=2\pi r/\lambda$) exceeds 100 [*Mishchenko et al*., 1998a, b]. However, its applicability is practically restricted to a rotationally symmetric particle, and thus this method is not used here. The discrete dipole approximation (DDA) is first developed by *Purcell and Pennypacker* [1973] and further developed by *Draine* [1988] and *Draine and Goodman* [1993]. DDA is suitable for the particle which has edges and whose radius is comparable to the wavelength of interest. Here we apply DDA to calculate the δ_p for perfectly cubic particles, which mimic sea-salt particles.

In DDA the particle is replaced by N subvolume elements, and each element is represented as an electric point dipole. Then the scattering problem can be solved numerically for this array of dipoles. Since DDA is an approximate theory, its solution contains some errors, and the applicability should be verified. The origin of the errors in the backscattering calculations by the DDA was investigated by *Okamoto et al*. [1995] and *Lemke et al*. [1998], and it turns out that the errors in the DDA is mainly caused by the insufficient representation of the target boundary by the discrete subvolume elements.

For a given size and refractive index of a target material, the accuracy of the DDA essentially depends on the number of dipoles and the shape. For the particle with edges, there are no analytical solutions, and backscattering by nonspherical particles have been recognized to be very difficult [*Bohren and Singham*, 1991]. Therefore the accuracy of the DDA for a cube is numerically investigated here by changing systematically the number of dipoles N for a given particle. Basically, the errors in DDA calculations with N dipoles for random orientations (i.e., the particle is oriented randomly in three-dimensional space in terms of the direction of incident radiation) is much smaller than those for a fixed orientation.

Here we use the N = 216,000 dipoles as a maximum number of dipoles due to the limitations of the computing resources. This reference DDA solution with N = 216,000 is assumed to be correct (in Figure 10a for copolarization and Figure 11a for cross polarization) to derive the dependence of errors in the DDA calculations on X and N. The calculations for copolarization is performed, and the results are shown in Figures 10a and 10b. The vertical axis in Figure 10a denotes the square of scattering matrix amplitude S_1 at backscattering direction which corresponds to the radiance for copolarization [*Bohren and Huffman*, 1983]. In a similar way the vertical axis in Figure 11a denotes the radiance for cross polarization. The horizontal axis expresses the volume equivalent size parameter X, which is defined as $X = 2\pi r_{\text{eff}}/\lambda$), and r_{eff} is the volume equivalent

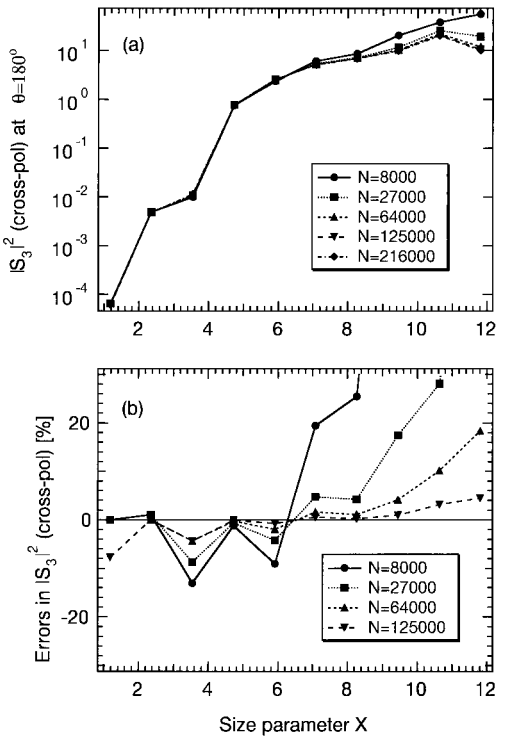

Figure 11. (a) Same as Figure 10a but for the cross-polarization signals. (b) Same as Figure 10b but for cross-polarization signals.

radius for a given cube; that is, $r_{\text{eff}} = 0.62a$ (a is the length of a side of a cube).

Relative errors for N, more than 10,000 dipoles, turn out to be very small, i.e., less than 10% for $X < 12$ (in Figure 10b). Similar analysis is also performed for cross polarizations. The errors for cross polarization is generally larger than those for copolarization for the particle modeled with the same number of dipoles N for the same X. However, overall accuracy for the DDA solutions with N > 10,000 is very good, i.e., errors for N = 27,000 to be smaller than 10% for $X = 8$ and those for N = 64,000 to be smaller than 10% for $X = 12$. Therefore we conclude that backscattering cross sections and depolarization ratios for X as large as 10 can be estimated by the DDA with an accuracy of 10% when particles are oriented randomly in three-dimensional space.

To derive depolarization ratios (Figure 12), which is expressed as $\delta_p = |S_3|^2/|S_1|^2$ for the analysis of lidar signals, we used N = 216,000 dipoles and assumed that cubic particles are oriented randomly as in the former calculations. The calculation shows that the δ_p arises at the size parameter X larger than about 4 (effective diameter > 0.8 μm) and takes the maximum of 22% at $x = 6 - 7$, then slowly decreases. Thus we can expect high δ_p (>10%) for crystallized NaCl particles, of which the effective size is larger than 1 μm. For the comparison with experimental results, we have to take into account the size distribution. However, the results of the presented calculation suggest that we have to take care of not only the shape but also the size of scattering particles when we discuss the depolarization ratio [*Mishchenko and Sassen*, 1998a].

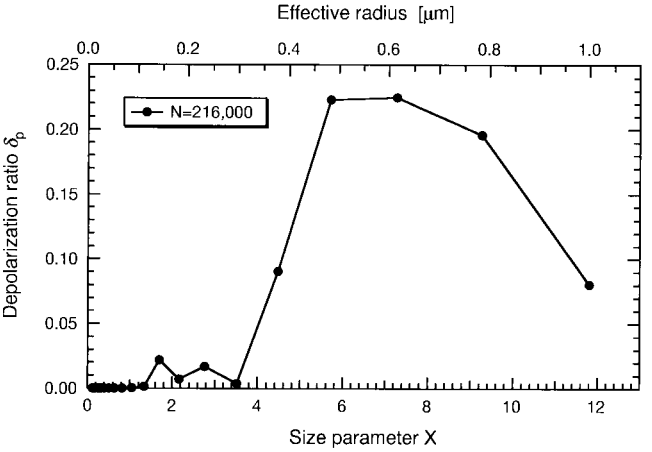

Figure 12. Depolarization ratios for cubic particles calculated by DDA.

5. Conclusions and Summary

We investigated the relatively high-depolarization events that occurred in the LA associated with sea breeze in the summer from July 16 to 19, 1996, by using lidar and Sun photometer measurements and a filter-sampling technique. Diurnal changes of the extinction coefficient (thus visibility) and the depolarization ratio in LA were correlated with sea-land breeze: sea breeze brings relatively clear air, but land breeze brings polluted air. The top of the relatively high δ_t layer rose to several hundred meters in the afternoon, which might reveal the development of ML or IBL.

It turned out that the chemical compositions of surface aerosols also had a large temporal variation. We found the diurnal change of the depolarization ratio in the LA and the successive changes of the surface aerosol components, mainly soil dust and sea-salt particles. The main sources of higher depolarization ratios are considered to be the local and/or transported dust indicated by Ca^{2+}(F, C) and crystallized sea-salt particles indicated by Na^{+}(C).

Simultaneous use of three different measurements (i.e., lidar and Sun photometer measurements and that of the filter-sampling technique) is quite fruitful to investigate the aerosol optical and chemical properties in the ABL and the dynamics of the boundary layer. Optical depth measured by a Sun photometer is useful to determine the average lidar ratio in lidar analysis. The influence of the choice of the boundary condition and the lidar ratio on lidar inversion analysis was examined, and it turned out that it is relatively small in the turbid atmosphere. We tentatively compared the lidar-derived extinction coefficient with PM_{10}. The average ratio was consistent with reported specific scattering coefficients. Most in situ monitoring, e.g., filter sampling of aerosols and measuring aerosol optical depth by the Sun photometer are usually carried out on the ground level. Thus the lidar, which is capable of producing reliable data around 100 m level as in the present case, should be useful for environmental monitoring.

We have presented a theoretical calculation for the perfect cubic particle based on the DDA for the first time with confidence of its accuracy, i.e., the error in depolarization ratio being less than 10%. The calculation confirmed that the crystallized NaCl particles larger than 1 μm in effective size cause a considerable (10–20%) depolarization ratio.

The structure revealed by the depolarization ratio in the LA apparently shows the lowest atmospheric boundary, which might reveal the ML or IBL and the height of sea breeze. It shows that the nonspherical particles, dust and crystallized sea-salt particles, were diffused in the layer. Thus the depolarization ratio measurement is useful for obtaining additional information on the boundary layer structure, which is not accessible by the lidar intensity profile only [e.g., *Sasano et al*., 1982], and to gain some insight into the composition of boundary layer aerosols and the generation mechanism of wind-driven aerosols.

Acknowledgments. This work is partly supported by the Grant-in-Aid for Scientific Research (C) 09640521 by the Ministry of Education, Science, Sports, and Culture and the joint research program of CEReS, Chiba University (9–14). We thank the Bureau of Environmental Protection, Tokyo Metropolitan Government, for providing the air pollution data. We appreciate the valuable comments made by the reviewers.

References

Angström, A., Techniques of Determining the Turbidity of the Atmosphere, *Tellus*, *13*, 214–223, 1961.

Banta, R. M., L. D. Oliver, and D. H. Levinson, Evolution of the Monterey Bay sea-breaze layer as observed by pulsed Doppler lidar, *J. Atmos. Sci*., *50*, 3959–3982, 1993.

Blanchard, D. C., and A. H. Woodcock, The production, concentration, and vertical distribution of the sea-salt aerosols, *Annals N. Y. Acad. Sci*., *330*, 1980.

Bohren, C. F., and D. R. Huffman, *Absorption and Scattering of Light by Small Particles*, 530 pp., John Wiley, New York, 1983.

Bohren, C., and S. B. Singham, Backscattering by nonspherical particles: A review of methods and suggested new approaches, *J. Geophys. Res*., *96*, 5269–5277, 1991.

Charlson R. J., N. C. Ahlquist, H. Selvidge, and P. B. MacCready Jr., *J. Air Pollut. Control Assoc*., *19*, 937–942, 1969.

Charlson R. J., S. E. Schwartze, J. M. Hales, R. D. Cess, J. A. Coakley Jr., J. E. Hansen, and D. J. Hofmann, *Science*, *255*, 423–430, 1992.

Cooper, D. W., J. W. Davis, and R. L. Byers, Measurements of depolarization by dry and humidified salt aerosols using a lidar analogue, *Aerosol Sci*., *5*, 117–123, 1974.

Draine, B. T., The discrete-dipole approximation and its application to interstellar graphite grains, *Astrophys. J*., *333*, 848–872, 1988.

Draine, B. T., and J. J. Goodman, Beyond Clausius-Mossotti:wave propagation on a polarizable point lattice and the discrete dipole approximation, *Astrophys. J*., *405*, 685–697, 1993.

Fernald, G. F., Analysis of atmospheric lidar observations: Some comments, *Appl. Opt*., *23*, 652–653, 1984.

Friedlander, S. K., *SMOKE, DUST AND HAZE: Fundamentals of Aerosols Behavior*, 317 pp., John Wiley, New York, 1977.

Garratt, J. R., *The Atmospheric Boundary Layer*, 316 pp., Cambridge University Press, New York, 1992.

Gillette, D. A., A wind tunnel simulation of the erosion of soil: Effect of soil texture, sand blasting, wind speed, and soil consolidation on dust production, *Atmos. Environ*., *12*, 1735–1743, 1978.

Gillette, D. A., I. H. Blifford Jr., and D. W. Fryrear, The influence of wind velocity on the size distributions of aerosols generated by the wind erosion of soils, *J. Geophys. Res*., *79*, 4068–4075, 1974.

Hidy, G. M., *AEROSOLS: An Industrial and Environmental Science*, 774 pp., Academic, San Diego, Calif., 1984.

Hoff, R. M., L. Guise-Bagley, R. M. Staebler, H. A. Wiebe, J. Brook, B. Georgei, and T. Düsterdiek, Lidar, meter, and in situ aerosol experiments in southern Ontario, *J. Geophys. Res*., *101*, 19,199–19,209, 1996.

Iwasaka, Y., M. Yamato, R. Imasu, and A. Ono, Transport of Asian dust (KOSA) particles: Importance of weak KOSA events on the geochemical cycle of soil particles, *Tellus*, *Ser. B*, *40*, 494–503, 1988.

Kai, K., K. Manome, M. Fujii, D. Muramatsu, M. Abo, C. Nagasawa, R. Murayama, Y. Ohono, T. Yokozawa, and H. Hara, The structure of the mixed layer and aerosol layer over Tokyo metropolitan area in summer, *Proc. Int. Laser Radar Conf*., *19th*, 131–134, 1998.

Klett, J. D., Stable analytical inversion solution for processing lidar returns, *Appl. Opt*., *20*, 211–220, 1981.

Lemke, H., H. Okamoto, and M. Quante, Comment on error analysis of backscatter from discrete dipole approximation for different ice particle shapes, *Atmos. Res*., *49*, 189–197, 1998.

Measures, R. M., *Laser Remote Sensing*, 510 pp., John Wiley, New York, 1984.

Mishchenko, M. I., and K. Sassen, Depolarization of lidar returns by small ice crystals: An application to contrails, *Geophys. Res. Lett*., *25*, 309–312, 1998a.

Mishchenko, M. I., and L. D. Travis, Capabilities and limitations of a current Fortran implementation of the T-matrix method for randomly oriented rotationally symmetric scatters, *J. Quant. Spectrosc. Radiat. Transfer*, *60*, 309–324, 1998b.

Miura, K., T. Kumakura, and T. Sekikawa, The effect of continental air mass on the modification of individual sea-salt particles collected over the coast and the open sea, *J. Meteorol. Soc. Jpn*., *69*, 429–438, 1991.

Miura, K., S. Nake, K. Aoki, S. Otagiri, and M. Ichikawa, Optical properties of aerosol particles over the Western Pacific Ocean, in *Proceedings of the 13th International Symposium on Remote Sensing*, Korean Soc. of Remote Sens., Pusan, 1997.

Murayama, T., M. Furushima, A. Oda, N. Iwasaka, and K. Kai, Depolarization ratio measurements in the atmospheric boundary layer by lidar in Tokyo, *J. Meteorol. Soc. Jpn*., *74*, 571–578, 1996.

Murayama, T., M. Furushima, A. Oda, and N. Iwasaka, Aerosol optical properties in the urban mixing layer studied by polarization lidar with meteorological data, in *Advances in Atmospheric Remote Sensing With Lidar*, edited by A. Ansmann, R. Neuber, P. Rairoux, and U. Wandinger, pp. 19–22, Springer-Verlag, New York, 1997.

Murayama, T., et al., Lidar network observation of Asian dust (Kosa) in Japan, *Proc. SPIE*, *3504*, 8–15, 1998a.

Murayama, T., N. Kaneyasu, H. Kamataki, S. Otsuka, M. Furihata, N. Iwasaka, and T. Tsukamoto, Monitoring of the atmospheric boundary layer with lidar, sun-photometer, and filter-sampling in Tokyo, *Proc. SPIE*, *3504*, 16–25, 1998b.

Murayama, T., H. Okamoto, and K. Miura, Lidar depolarization ratio in the lower atmosphere: Measurement, theory, and analysis, paper presented at Conference on Light Scattering by Nonspherical Particles: Theory, Measurements, and Applications, Am. Meteorol. Soc., New York, Sept. 29–Oct. 1, 1998c.

Nakane, H. and Y. Sasano, Structure of a sea-breeze front reveled by scanning lidar observation, *J. Meteorol. Soc. Jpn*., *64*, 787–791, 1986.

Ohta, S., and T. Okita, Measurements of particulate carbons in urban and marine air in Japanese areas, *Atmos. Environ*., *18*, 2439–2445, 1984.

Okamoto, H., A. Macke, M. Quante, and E. Raschke, Modeling of backscattering by non-spherical ice particles for interpretation of cloud radar signals at 94 GHz, An error analysis, *Beitr. Phys. Atmos*., *68*, 319–334, 1995.

Perry, R. J., A. J. Hunt, and D. R. Huffman, Experimental determinations of Mueller scattering matrices for nonspherical particles, *Appl. Opt*., *17*, 2700–2710, 1978.

Purcell, E. M., and C. R. Pennypacker, Scattering and absorption of light by nonspherical dielectric grains, *Astrophys. J*., *186*, 705–714, 1973.

Quinby-Hunt, M. S., L. L. Erskine, and A. J. Hunt, Polarized light scattering by aerosols in the marine atmospheric boundary layer, *Appl. Opt*., *36*, 5168–5184, 1997.

Sasano, Y., and H. Nakane, Significance of the extinction/backscatter ratio and the boundary value term in the solution for the two-component lidar equation, *Appl. Opt*., *23*, 11–13, 1984.

Sasano, Y., A. Shigematsu, H. Shimizu, N. Takeuchi, and M. Okuda, On the relationship between the aerosol layer height and the mixed layer height determined by laser radar and low-level radiosonde observations, *J. Meteorol. Soc. Jpn*., *60*, 889–895, 1982.

Sassen, K., The polarization lidar technique for cloud research: A review and current assessment, *Bull. Am. Meteorol. Soc*., *72*, 1848–1866, 1991.

Sassen, K., The lidar backscatter depolarization technique for cloud and aerosol research, in *Light Scattering by Nonspherical Particles: Theory, Measurements, and Geophysical Applications*, edited by M. L. Mishchenko, J. W. Hovenier, and L. D. Travis, Academic, San Diego, Calif., in press, 1999.

Takamura, T. Y. Sasano, and T. Hayasaka, Tropospheric aerosols optical properties derived from lidar, sun photometer, and optical particle counter measurements, *Appl. Opt*., *33*, 7132–7140, 1994.

Tang, I. N., Chemical and size effects of hygroscopic aerosols on light scattering coefficients, *J. Geophys. Res*., *101*, 19,245–19,250, 1996.

Tang, I. N., H. R. Munkelwitz, and J. G. Davis, Aerosol growth studies, II, Preparation and growth measurements of monodisperse salt aerosols, *J. Aerosol Sci*., *8*, 149–159, 1977.

Winker, P., and C. E. Junge, Comments on "Anomalous deliquescence of sea spray aerosols," *J. Appl. Meteorol*., *10*, 159–163, 1971.

Young, A. T., Revised depolarization corrections for atmospheric extinction, *Appl. Opt*., *19*, 3427–3428, 1980.

H. Kamataki, Tokyo Metropolitan Research Institute for Environmental Protection, Koto, Tokyo, Japan.

N. Kaneyasu, National Institute of Resources and Environment, Tsukuba, Ibaraki, Japan.

K. Miura, Department of Physics, Science University of Tokyo, Shinjuku, Tokyo, Japan.

T. Murayama, Dep. of Physics, Tokyo University of Mercantile Marine 2-1-6 Etchujima, Koto, Tokyo, Japan. (e-mail: murayama@ipc.tosho-u.ac.jp)

H. Okamoto, Kashima Space Research Center, Communications Research Laboratory, Kashima, Ibaraki, Japan.

(Received January 21, 1999; revised May 20, 1999;
accepted June 23, 1999.)